MATERIALS SCIENCE

Bulk ultrafine grained/nanocrystalline metals via slow cooling

Chezheng Cao[1,2], Gongcheng Yao[1,2], Lin Jiang[3,4], Maximilian Sokoluk[2], Xin Wang[3], Jim Ciston[5], Abdolreza Javadi[2], Zeyi Guan[2], Igor De Rosa[1], Weiguo Xie[6], Enrique J. Lavernia[3], Julie M. Schoenung[3], Xiaochun Li[1,2]*

Cooling, nucleation, and phase growth are ubiquitous processes in nature. Effective control of nucleation and phase growth is of significance to yield refined microstructures with enhanced performance for materials. Recent studies reveal that ultrafine grained (UFG)/nanocrystalline metals exhibit extraordinary properties. However, conventional microstructure refinement methods, such as fast cooling and inoculation, have reached certain fundamental limits. It has been considered impossible to fabricate bulk UFG/nanocrystalline metals via slow cooling. Here, we report a new discovery that nanoparticles can refine metal grains to ultrafine/nanoscale by instilling a continuous nucleation and growth control mechanism during slow cooling. The bulk UFG/nanocrystalline metal with nanoparticles also reveals an unprecedented thermal stability. This method overcomes the grain refinement limits and may be extended to any other processes that involve cooling, nucleation, and phase growth for widespread applications.

INTRODUCTION

Cooling, nucleation, and phase growth are ubiquitous processes of paramount significance in almost every aspect of life and landscape in nature, such as cloud formation (1), ice nucleation (2), and volcanic rock evolution (3). It is universally established that effective control of nucleation and phase growth will yield refined microstructures with enhanced performance for materials, and hence is vital to numerous broad fields, including materials science, climate and atmospheric sciences, biomedicine (4), and chemistry (5). Widely used technologies that involve cooling, such as casting, are of significance for the mass production of complex materials and components. Recent studies reveal that ultrafine grained (UFG)/nanocrystalline metals exhibit extraordinary properties (6–8). However, it has been considered impossible to fabricate bulk UFG/nanocrystalline metals by casting, a technology that has been used for over 6000 years, partly due to its slow cooling (e.g., less than 100 K/s). Conventional microstructure refinement methods, such as fast cooling (thousands to millions of kelvin per second) and inoculation, have reached certain fundamental or technical limits (9–12). Fast cooling substantially restricts the size and complexity of the as-solidified materials. The minimum grain size achievable by inoculation in casting falls in the range of tens of micrometers.

Grain refinement in metals during solidification is of great interest due to the enhanced mechanical properties, more homogeneous microstructure, and improved processability of refined microstructures. Over the past few decades, different approaches such as inoculation (13–15), growth restriction by adding alloy elements (16, 17), and fast cooling (up to 10^7 K/s) (18, 19) have been widely investigated through both theoretical and experimental pathways in an effort to attain optimal grain refinement effects. However, these approaches have failed to demonstrate whether it is possible to cast UFG/nanocrystalline metals by the conventional casting process, which would represent a revolutionary approach given the pervasiveness of casting in manufacturing. As a consequence of our inability to implement solidification processes to fabricate UFG/nanocrystalline metals, various methods have emerged for the fabrication of UFG/nanocrystalline metals, including mechanical alloying (20, 21), severe plastic deformation (6–7, 22), and thin-film deposition (23, 24), and although some degree of success has been achieved using these processes, they remain limited to the solid state and present challenging issues for economical mass production of bulk samples with complex geometries. Recent work has shown that the solidification behavior of metals can be controlled by the addition of nanoparticles (12, 25–28). These studies about nanoparticle-controlled solidification have paved a new pathway for casting metals with refined microstructures.

Here, we report a new discovery that nanoparticles can refine metal grains down to ultrafine or even nanoscale by instilling a continuous nucleation and growth control mechanism during slow solidification. When casting pure Cu with tungsten carbide (WC) nanoparticles, the grain sizes of Cu are refined substantially down to ultrafine and even nanoscale. The as-solidified bulk ultrafine/nanocrystalline Cu reveals an unprecedented thermal stability up to 1023 K (0.75 melting point of Cu) and high mechanical properties. Furthermore, this newly revealed grain control mechanism is successfully applied in other materials systems such as Al-TiB$_2$ and Zn-WC for ultrafine grains via slow cooling. This revolutionary method paves the way for the mass production of bulk stable UFG/nanocrystalline materials that may be readily extended to any other processes that involve cooling, nucleation, and phase growth for widespread applications.

RESULTS AND DISCUSSION

Nanoparticle incorporation and dispersion in bulk samples

We prepared bulk Cu ingots with WC nanoparticles using two different methods. The first method is a salt-assisted self-incorporation of nanoparticles into molten metal (see Materials and Methods). As shown in fig. S1A, molten salt (Borax + 5% CaF$_2$) could dissolve the oxide layer at the top of molten metal and provide a clean interface

[1]Department of Materials Science and Engineering, University of California, Los Angeles, Los Angeles, CA 90095, USA. [2]Department of Mechanical and Aerospace Engineering, University of California, Los Angeles, Los Angeles, CA 90095, USA. [3]Department of Materials Science and Engineering, University of California, Irvine, Irvine, CA 96297, USA. [4]Materials & Structural Analysis, Thermo Fisher Scientific, Hillsboro, OR 97124, USA. [5]National Center for Electron Microscopy, Molecular Foundry, Lawrence Berkeley National Laboratory, Berkeley, CA 94720, USA. [6]Camborne School of Mines, University of Exeter, Penryn Campus, Penryn, Cornwall TR10 9FE, UK.
*Corresponding author. Email: xcli@seas.ucla.edu

between the Cu melt and the nanoparticles. In addition, the wetting angle between Cu and WC at 1250°C is below 10° (*29*), which indicates a good wettability between Cu and WC so that WC nanoparticles prefer to transport from the molten salt to the Cu melt to reduce the system energy (*27*, *30*). Combined with mechanical mixing, WC nanoparticles can be readily incorporated into molten Cu. This salt-assisted incorporation method opens up a scalable manufacturing method to fabricate metals containing different percentages of nanoparticles. In this study, bulk Cu ingots with 5, 10, and 20% volume fraction of WC nanoparticles were cast. Another method is a powder melting process (see Materials and Methods) especially suitable for high-volume percent of nanoparticles, as shown in fig. S1B. The cold compacted Cu-WC powder preform was melted with an induction heater under a pressure of 7 to 10 MPa. Cu ingots with 19 and 34% volume fraction of WC nanoparticles were fabricated by this powder melting method. Note that the second method is not as scalable as the first method but is more suitable for a high-volume loading of nanoparticles, if needed.

To study the effects of the cooling rate under the same initial condition, we melted all these Cu-WC samples again and casted them under different cooling rates, i.e., furnace cooling (2 to 4 K/s), air cooling under the protection of argon gas (7 to 12 K/s), and water quenching (70 to 100 K/s). The typical cooling curves are shown in fig. S2, and the thermal arrest caused by the solidification of Cu is identified in the furnace and air cooling curve but is not obvious in the water quenching curve due to the rapid heat dissipation.

Grain structure characterization

We then characterized the distribution and dispersion of WC nanoparticles and grain structures in cast bulk Cu samples by scanning electron microscopy (SEM), transmission electron microscopy (TEM), focused ion beam (FIB) imaging, scanning TEM (STEM), and electron backscatter diffraction (EBSD). SEM samples were sectioned along the cross-section of the sample. To reveal the nanoparticles, we further polished the mechanically ground and polished samples by low-angle ion milling at 4° for 1.5 hours.

The inset in Fig. 1A shows one typical bulk Cu-WC ingot cast after the salt-assisted incorporation method. Figure 1A shows the typical SEM microstructure of Cu-5vol%WC by furnace cooling acquired at 52°. WC nanoparticles are uniformly dispersed in the Cu matrix. Our theoretical analysis, detailed in the "Nanoparticle dispersion and self-stabilization mechanism" section of the Supplementary Materials, shows that the excellent wettability between Cu and WC can stabilize the dispersed nanoparticles in the metal melt. The average size of WC nanoparticles was measured to be approximately 200 nm in diameter, as shown in fig. S3. The UFG microstructure of
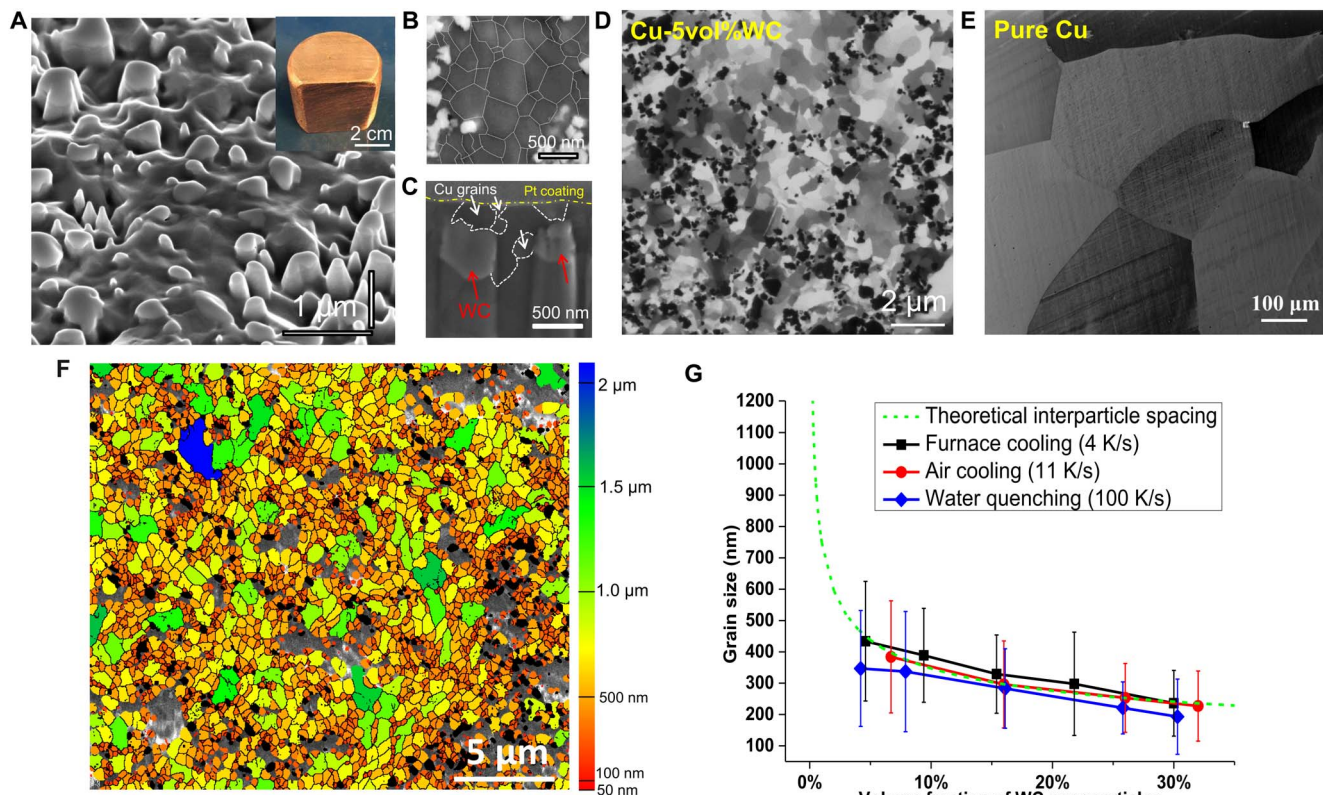

Fig. 1. Microstructure of bulk UFG/nanocrystalline Cu-containing distributed WC nanoparticles. (**A**) SEM image of Cu-5vol%WC (by a cooling rate of 4 K/s) acquired at 52° showing well-dispersed WC nanoparticles in the Cu matrix. Inset is the image of a typical as-cast bulk Cu-5vol%WC ingot with a diameter of 50 mm. (**B**) Magnified SEM image of Cu-5vol%WC (4 K/s) showing the ultrafine and nanoscale Cu grains. (**C**) SEM image of the cross-section showing the UFG Cu matrix and the WC nanoparticles present beneath the surface of the sample. (**D**) Typical FIB image of Cu-5vol%WC (4 K/s) showing the UFG/nanocrystalline microstructure. (**E**) FIB image of pure Cu cast under the same condition showing coarse Cu grains. (**F**) EBSD image of Cu-5vol%WC (4 K/s) with grain size color code. Black phases are WC nanoparticles, red grains are smaller than 100 nm, and yellow and orange grains are smaller than 1 μm. (**G**) Summary of the average Cu grain sizes for different volume fractions of nanoparticles under different cooling rates. Error bars show the SD.

Cu-5vol%WC (4 K/s) is shown in the SEM image of Fig. 1B (Cu grains marked by white dashed lines). Grains in this SEM image are smaller than 1000 nm. Note that some areas without nanoparticles from a top view under SEM may have nanoparticles beneath the surface, as shown in the SEM image of Fig. 1C, showing the cross-section cut by FIB. Cu grains are pinned by nanoparticles beneath the surface. Pt coating is used to protect the Cu surface during the FIB cutting. The channeling contrast of different grains induced by ion beam makes FIB a powerful tool to characterize grain structures. Figure 1 (D and E) shows the typical ion beam micrographs of Cu-5vol% WC and pure Cu cast under the same casting condition (2 to 4 K/s), respectively. The dark phase in Fig. 1D corresponds to WC nanoparticles, whereas the white or grayish phases indicate the Cu grains. More FIB images of as-cast Cu-WC samples with 5, 10, and 20 volume % of WC nanoparticles are shown in fig. S4 (A to C). With the addition of WC nanoparticles into Cu, the grain sizes are readily refined to ultrafine and even nanoscale. From the FIB micrographs, we can observe that a higher percentage of nanoparticles yield more dense nanoparticle distribution and thus more refined grain microstructures. For comparison, the as-solidified pure Cu sample, however, has an average grain size of 270 ± 132 μm under the same cooling rate.

EBSD analysis was used to further investigate the grain sizes. Figure 1F shows the typical EBSD micrograph of Cu-5vol%WC cast by a cooling rate of 4 K/s. The black phases correspond to the WC nanoparticles. Because the surfaces of nanocomposite samples were not perfectly flat (nanoparticles stick out from the matrix) after ion milling, some regions (marked as grayish region) were not able to be identified during the EBSD scanning. The colors of different grains correspond to different sizes, as shown in the legend. Red grains are smaller than 100 nm, yellow and orange grains are smaller than 1 μm, while green and deep blue grains are smaller than 2 μm. Most of the Cu grains are smaller than 1 μm, and a substantial number of nanosized Cu grains (marked with red color in the EBSD micrograph) can be observed in the nanoparticle-rich areas. The average grain sizes of different areas under different cooling rates are summarized in Fig. 1G. The average grain size of Cu-WC samples with different fractions of WC nanoparticles ranges from 236 to 434 nm, 227 to 384 nm, and 193 to 347 nm for furnace cooling, air cooling, and water quenching, respectively. The error bars indicate the SD of the grain size measurements. It is shown that a higher percentage of nanoparticles yields more refined grains. Figure 1G also indicates that the grain size slightly decreases with an increased cooling rate, although the differences from the cooling rates are not obvious. The EBSD scanning also supports that the addition of WC nanoparticles can refine Cu grains to ultrafine/nanoscale by regular casting.

If we assume that nanoparticles are spherical and homogeneously distributed in the matrix, then the theoretical center-to-center interparticle spacing between WC nanoparticles could be calculated by

$$d = r\left(\frac{4\pi}{3f_v}\right)^{\frac{1}{3}}$$

where d is the theoretical center-to-center interparticle spacing, r is the radius of the particles (e.g., about 100 nm in this case), and f_v is the volume fraction of particles. The green dotted line in Fig. 1G corresponds to the theoretical interparticle spacing of the WC particles at different volume fractions. Note that the experimental results for Cu grain sizes are close to the theoretical interparticle spacing between nanoparticles. Figure S5 shows the STEM image of

the nanoparticle-rich area, which suggests that the Cu grain size is correlated to the WC interparticle spacing. The equation also suggests that a smaller nanoparticle would only need a lower volume fraction to make smaller grains as long as the nanoparticles are not engulfed. Lower cooling rates actually favor the non-engulfment (pushing) of nanoparticles during solidification.

Nucleation and grain growth control

To further provide fundamental insight into the underlying nucleation and grain growth phenomena, we conducted differential scanning calorimetry (DSC) studies, and the typical cooling curves at a cooling rate of 5°C/min of pure Cu and Cu with WC nanoparticles (samples have the same mass, 50 mg) are shown in Fig. 2A (see more details in Materials and Methods and fig. S6). The bump on the cooling curve of the pure Cu sample corresponds to the exothermal peak from the solidification of Cu that started at 1033°C, which indicates that a 51°C undercooling is needed to activate major nucleation of Cu grains. However, the starting point of the exothermal peak of Cu-10vol% WC is 1078°C, which means that only a 6°C undercooling was needed by the addition of WC nanoparticles. The undercooling difference indicates that the WC nanoparticle is a relatively potent nucleation particle for Cu. For effective nucleation, the crystallographic lattice discrepancy between the particles and the matrix is crucial for the nucleation; thus, the interface between the matrix and the nanoparticles was studied at the atomic scale by high-resolution TEM. Figure 2B shows the typical interface between the WC nanoparticles and the Cu matrix at the atomic scale. Figure 2C is the Fourier-filtered atomic-resolution TEM image at the marked area of Fig. 2B. The atomic structure indicates a clean and well-matched Cu-WC interface, with no intermediate phases present. The top-right and bottom-left insets are the fast Fourier transformation of the Cu matrix and the WC nanoparticles, respectively. It is identified that the (10$\bar{1}$1) planes of WC nanoparticles are parallel with (200) planes of the Cu matrix. The plane distances of (200) Cu and (10$\bar{1}$1) WC are 0.1806 and 0.1881 nm, respectively. Thus, the misfit is calculated to be 4.1%, which implies a coherent lattice matching at this specific interface. The presence of a clean and coherent interface suggests a strong interfacial bond. The coherent interface indicates that WC nanoparticles could serve as potent nucleation sites for Cu grains.

Moreover, the number of potential nucleation sites (WC nanoparticles) in the Cu-WC sample is significantly higher than that in a conventional inoculation method. It is known that nanoparticles can serve as effective nucleation sites due to their high number density (31). For example, the population density of particles for 5 parts per thousand (ppt) Al-5Ti-1B refiner is around 5×10^{14} m^{-3} (9). In comparison, the population densities of WC nanoparticles are calculated to be 1.2×10^{19}, 2.4×10^{19}, and 4.8×10^{19} m^{-3} (assuming that WC nanoparticles are spherical) for Cu-5vol%WC, Cu-10vol%WC, and Cu-20vol%WC samples, respectively. The population densities of nanoparticles are five orders of magnitude higher than those of the popular Al-Ti-B grain refiner.

Following the initial nucleation of grains from the melt, the nucleated grains grow rapidly and release latent heat, which usually prevents the nucleation of new grains nearby. In contrast, with nanoparticles in the molten metal, nanoparticles can rapidly assemble/adhere to the solid-liquid interface to effectively restrict the grain growth, preventing other potential nucleation sites from being suppressed by the latent heat release. Therefore, later nucleation events could occur continuously during the solidification, which is crucial for this new grain refinement and growth control mechanism. This
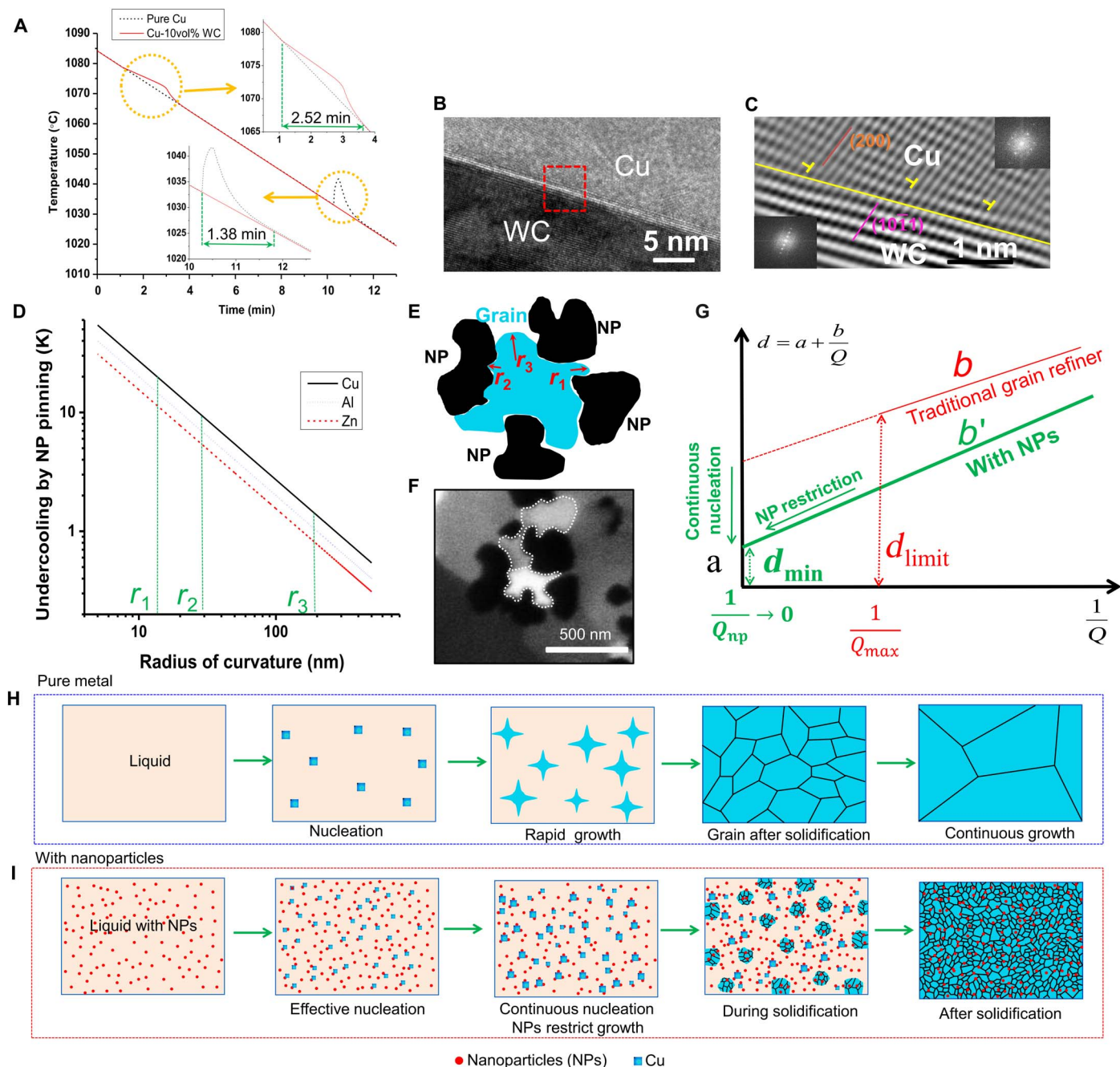
Fig. 2. Nucleation and grain growth control mechanisms by nanoparticles. (**A**) Typical DSC scanning result during the cooling of pure Cu and Cu-10vol%WC. (**B**) Typical TEM image of the Cu-WC interface showing the interface between the Cu matrix and the WC nanoparticle. (**C**) Fourier-filtered high-resolution TEM image of the marked red rectangle area in (B) showing a characteristic interface between the WC nanoparticle and the Cu matrix. Insets are the fast Fourier transformation of the Cu matrix (top right) and the WC nanoparticle (bottom left). (**D**) Undercooling requirement to overcome Gibbs-Thompson pinning effect for Cu, Al, and Zn. (**E**) Schematic illustration of the nanoparticle pinning effects. (**F**) SEM image of a Cu grain refined by WC nanoparticles. (**G**) Nanoparticles break the fundamental limit that existed in conventional grain refinement methods. (**H** and **I**) Schematic illustrations of phase evolution during solidification of pure metal (H) and metal with nanoparticles (I).

growth restriction and continuous nucleation can be validated by comparing the width of the exothermal peaks of pure Cu and Cu with nanoparticles in the DSC study. Figure 2A indicates that the Cu-10vol%WC sample took an 83% longer time to complete the solidification. The heat flow curves during DSC tests were shown in fig. S6. The exothermal peaks correspond to the latent heat release from the solidification.

The width of the peak in pure Cu is 6.9°C, while it is 12.6°C in the Cu-10vol%WC sample, which means that the exothermal peak in pure Cu is sharp and intensive, and is gradual and wide in Cu-WC samples. These results suggest that the nanoparticles are able to slow down solidification and enable a continuous nucleation and an effective grain growth control during solidification.

It is well known that, after nucleation, grain growth control during solidification is vital to achieve refined grain structures. It is proposed here that nanoparticles will impede grain growth during solidification by forcing the solidification front to grow with a nonlinear geometry (e.g., curved solidification front). When Cu grains form curvatures with a small radius during solidification, the free energy (Gibbs-Thomson effect) increases. The molar free energy increase can be calculated by

$$\Delta G_\gamma = \frac{2\gamma V_m}{r}$$

where ΔG_γ is the molar free energy increase, γ is the interfacial energy of the interface, V_m is the molar volume of the phase, and r is the radius of curvature of the interface. If this increment of free energy is large enough (thus, larger undercooling is needed), then the growth of Cu grains may be inhibited (12). The undercooling needed to overcome a curved interface generated by nanoparticle pinning can be described by the Gibbs-Thompson effects and can be calculated by

$$\Delta T = \frac{2\gamma T_m}{r H_f}$$

where γ is the interface energy of solid-liquid interfaces (Cu, 0.185 J/m^2; Al, 0.116 J/m^2; Zn, 0.09 J/m^2), T_m is the melting temperature of the metal, r is the radius of curvature of the solidification front, and H_f is the enthalpy of fusion. The undercooling needed to overcome the grain front curvatures when pinned by nanoparticles for Cu, Al, and Zn is shown in Fig. 2D.

As shown in the schematic illustration (Fig. 2E) of the nanoparticle pinning effects, there are mainly two types of curvature generated by nanoparticles: (i) Marked as r_1 and r_3 in Fig. 2E, when a solidification front meets with dispersed nanoparticles, the Cu phase can grow through the micro/nanochannels between nanoparticles and form a curvature with a small radius that results in an increase of free energy (Gibbs-Thomson effect). (ii) Marked as r_2 in Fig. 2E, nanoparticles have curved surfaces, and when Cu solidification front meets nanoparticles, the curvature at the interface between Cu and WC nanoparticles will need extra undercooling to remain solid. The range of the undercooling needed by the curvatures generated by nanoparticle pinning effects is a few tens of kelvin, as marked by r_1, r_2, and r_3 in Fig. 2D. The curvatures generated by nanoparticles are observed in the SEM image as shown in Fig. 2F. The Cu grain is surrounded by several WC nanoparticles and shows both types of curvatures as mentioned above.

On the basis of classic theories for nucleation and grain growth in alloys, it is well recognized that grain growth velocity can be reduced by the solute atoms at the solid-liquid interface during alloy solidification. Published studies have revealed an empirical relationship (as shown in Fig. 2G) between the average grain size (d) and the restriction factor Q (17, 18) for alloys

$$d = a + \frac{b}{Q}$$

where a is a constant related to the number of particles that actually nucleate grains at infinite values of Q. In the ideal case, when Q is infinitely large, the grain size could be refined to a, which is dictated by interparticle spacing. b is a constant related to the potency of the nucle-

ation particles. Q is the restriction factor, which is inversely proportional to the constitutional undercooling, traditionally defined as

$$Q = mC_0(k-1)$$

where m is the liquidus slope in a linear phase diagram, C_0 is the solute content in the alloy, and k is the equilibrium solute partition coefficient. From the definition of Q, we can see that the restriction factor is determined by the phase diagram and the specific chemical composition of the specific alloy. Thus, the chemical restriction from solute atoms is very limited. It has been reported that the maximum value of Q (Q_{max}) in some practical alloys can be around 50 K (18, 25). As shown in Fig. 2G, with a limited Q_{max}, the smallest grain size achievable by traditional inoculation and solute atoms is d_{limit}, which is approximately tens of micrometers.

In contrast, here, we proposed that nanoparticle pinning can induce a new restriction factor, Q_{np}, which can break the fundamental limits sets by Q that depends on constitutional undercooling. The nanoparticle-enabled grain growth restriction can extend the chemical restriction factor Q to a physical restriction factor Q_{np}, which could be readily increased to a large number, if not infinity (see the "Growth restriction factor by nanoparticles" section of the Supplementary Materials and fig. S8). Moreover, populous nanoparticles (five orders of magnitude more) could serve as potent nucleation sites in the continuous nucleation; thus, a (related to the number of effective nucleation sites) is significantly reduced. The average grain size can be reduced to d_{min} when $1/Q_{np}$ approaches zero. We propose that d_{min} achievable is determined by the theoretical interparticle spacing. The trend line of theoretical interparticle spacing in Fig. 1G is consistent with our experimental data of average grain sizes in Cu-WC samples. This indicates that nanoparticle-enabled continuous nucleation and grain growth control could enable us to refine grains down to the interparticle spacing limit under slow cooling. Therefore, nanoparticles effectively break the fundamental limits set by the conventional solidification process and readily refine grains down to ultrafine or even nanoscale by the regular casting process. On the basis of the experimental results and theoretical analysis, the mechanisms of nanoparticle-enabled grain refinement and control, in comparison to the classic grain refinement, during regular casting are schematically illustrated in Fig. 2 (H and I).

Other less dominant mechanisms may also play minor roles in phase growth control, such as blocking of the diffusion of atoms to the surface of the growing phase and modification of the local temperature field by nanoparticles. Nanoparticles can remain at the solidification front and block the transportation of the atoms, thus slowing down the grain growth (19, 25–27). When the density of nanoparticles is low, this effect will not play a major role. Moreover, when WC nanoparticles are close to the solidification front, the nanoparticles could affect the local thermal fields. The lower thermal conductivity of ceramic nanoparticles could slow down the transportation of latent heat from the solidification front and protect potential nucleation sites.

Other materials systems

The nanoparticle-enabled grain refinement has also been validated for other materials systems. Al-TiB$_2$ and Zn-WC were also studied to determine whether it is possible to achieve UFG/nanocrystalline microstructures via slow cooling for different metals. The salt-assisted self-incorporation method (see Materials and Methods) was used to fabricate Al containing 10 volume % TiB$_2$ nanoparticles (with an average size of about 100 nm) by furnace cooling (0.7 K/s as measured).

Figure 3A shows the FIB image of Al-10vol%TiB$_2$, the dark phases are TiB$_2$ nanoparticles, while the gray matrix is Al. TiB$_2$ nanoparticles are reasonably well dispersed in the Al matrix. The higher magnified image is shown in Fig. 3B. We can identify Al grains (marked by white dashed lines and pink arrows) smaller than 1.0 μm surrounded by TiB$_2$ nanoparticles (marked by yellow arrows). The TEM image of Fig. 3C demonstrates one ultrafine Al grain (marked by white dashed lines) that has been controlled by several TiB$_2$ nanoparticles. The grain size distribution of Al is shown in Fig. 3D with an average grain size of 460 ± 220 nm. Zn-5vol%WC samples were also fabricated by casting with a cooling rate of 3.7 K/s (see Materials and Methods). As shown in Fig. 3 (E and F) (SEM images of Zn-5vol%WC), WC nanoparticles are distributed and dispersed in the Zn matrix. Zn grains (marked by white dashed lines and pink arrows) close to 1.0 μm are identified. The FIB image of Fig. 3G shows a better contrast from the Zn grains. The size distribution of Zn grains is shown in Fig. 3H with an average grain size of 991 ± 746 nm. It is thus validated that Zn grains were refined to approximately 1.0 μm by the addition of 5 volume % WC nanoparticles, although the grain refinement is not as effective as in the Cu and Al cases. The reason is mainly due to the smaller undercooling required to overcome the Gibbs-Thompson pinning effects for Zn than for Al and Cu, as shown in Fig. 2C. This nanoparticle-enabled grain refinement approach provides an additional general pathway to produce UFG/nanocrystalline metals by regular casting.

Thermal stability

The thermal stability of UFG/nanocrystalline metals is another grand challenge that limits their widespread use in many applications. It has been reported that pure nanocrystalline metals (Al, Cu, Sn, Pb, Zn, and Mg) exhibit extensive grain growth even at room temperature (~300 K). Nanocrystalline metals with higher melting points (~1700 K), such as Co, Ni, and Fe, see a rapid grain growth over a moderate temperature range of 220° to 450°C (493 to 723 K), resulting in micrometer-sized grains at temperatures less than a half of their melting temperatures (32, 33). Approaches that involve adding solute atoms to stabilize nanocrystalline metals by pinning the grain boundaries or lowering the grain boundary energy have yielded some successful results (34, 35). However, these approaches remain inherently limited by the thermodynamic properties of the particular alloy systems. It is proposed that dispersed nanoparticles could stabilize the UFG/nanocrystalline metals at elevated temperatures. To study the nanoparticle-enabled stabilization in the as-cast Cu-WC nanocomposites at elevated temperatures, we further investigated the grain growth using STEM equipped with in situ heating capability. The in situ heating path stays at 200°, 400°, and 600°C for 10 min and at 850°C for 30 min. Figure 4 (A and E) shows the local microstructures of as-solidified Cu-WC samples with different local volume percentages of nanoparticles. The local nanoparticle concentration in Fig. 4A is higher than that in Fig. 4E. The relatively bright phases are WC nanoparticles, and the black phase is the Cu matrix. The grain structures at 400°, 600°, and 850°C shown in Fig. 4 (B to D and F to H) are acquired at longer camera lengths than those shown in Fig. 4 (A and E) to enhance the diffraction contrast of the image to distinguish individual Cu grains. In the nanoparticle-rich local area, Fig. 4 (A to D) shows that nanoscale grains were thermally stable at temperatures up to 850°C (Fig. 4D). The grain sizes in the nanoparticle-dense zone at 25°, 400°, 600°, and 850°C are 114 ± 20, 123 ± 31, 157 ± 40, and 197 ± 98 nm, respectively. In the area with fewer nanoparticles (Fig. 4, E to H), ultrafine/nanoscale grains were thermally stable up to about 600°C. The grain sizes in the nanoparticle-less zone at 25°, 400°, 600°, and 850°C are 134 ± 27, 160 ± 49, 209 ± 59, and 269 ± 79 nm, respectively. When the temperature was raised to 850°C, ultrafine/nanoscale grains started to grow significantly and became larger grains (Fig. 4H). Although we
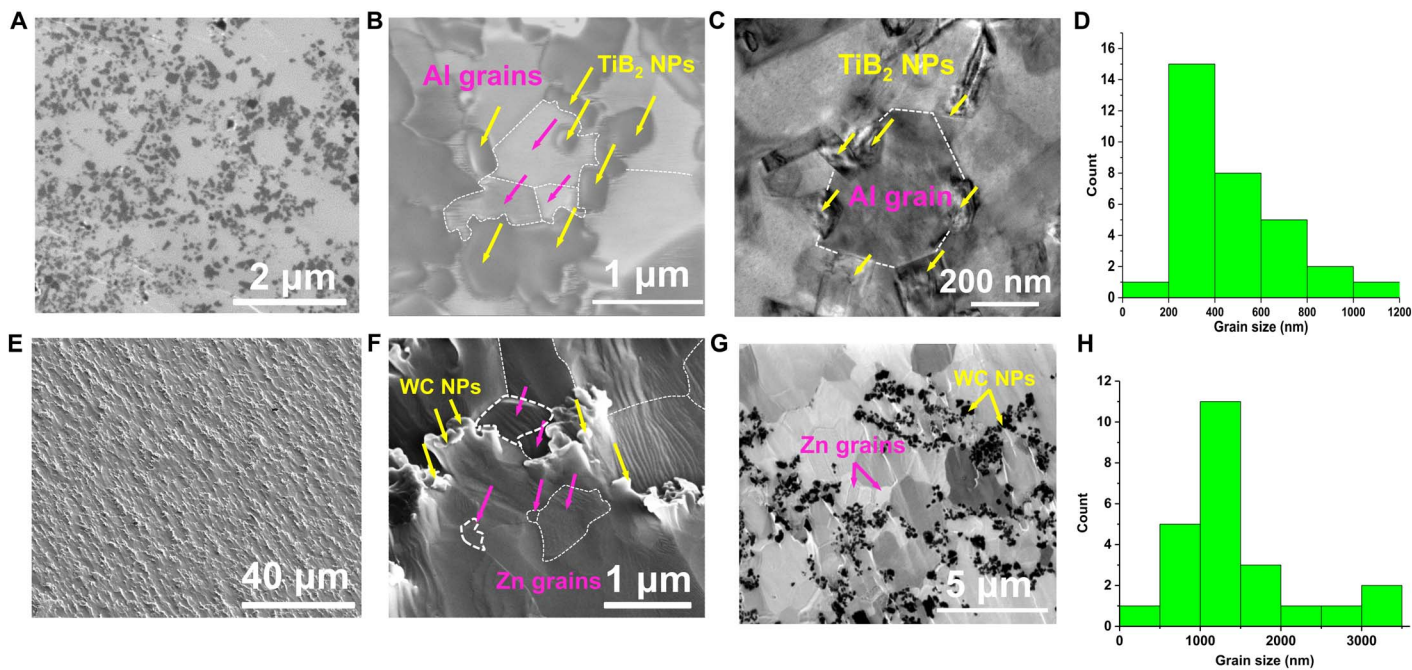

Fig. 3. Nanoparticle-enabled grain refinement in other materials systems. (**A** and **B**) FIB images of Al-10vol%TiB$_2$ cast by furnace cooling (0.7 K/s) showing the distribution of TiB$_2$ nanoparticles and ultrafine Al grains. (**C**) TEM image of Al-10vol%TiB$_2$ (0.7 K/s) showing one ultrafine Al grain surrounded by TiB$_2$ nanoparticles. (**D**) Al grain size distribution of Al-10vol%TiB$_2$ (0.7 K/s). (**E** and **F**) SEM image of Zn-5vol%WC by air cooling (3.7 K/s). (**G**) FIB image of Zn-5vol%WC (3.7 K/s). (**H**) Zn grain size distribution of Zn-5vol%WC (3.7 K/s).

observed grain growth at elevated temperatures, this growth was restricted by nanoparticles close to this area, and therefore, the grain sizes did not exceed the UFG size. This restriction indicates that nanoparticles effectively inhibit grain growth in the solid state up to a temperature of 850°C (1123 K), which significantly corresponds to approximately 0.83 of the melting temperature of Cu (1353 K).

To further validate the thermal stability of the refined Cu grains and study the effects on mechanical properties by heat treatment, we heated the Cu-34vol%WC sample obtained by casting under air cooling (cooling rate of 7 K/s), which had an average grain size of 208 ± 94 nm, to 750°C (1023 K, 0.75 of the melting point of Cu) and held the sample at this temperature for 2 hours under the protection of argon. Figure 4I shows a typical SEM image of the Cu-34vol%WC sample after the high-temperature exposure. EBSD was used to study the potential grain growth in the nanoparticle-poor zone such as the marked white rectangle area in Fig. 4I. Figure 4J shows that most Cu grains are still smaller than 1.0 μm, while a substantial number of nanoscale grains remained after the heat treatment. The grain size distribution in Fig. 4K confirms that the average Cu grain size is 248 ± 135 nm after the heat treatment, which is close to the average grain size, 208 ± 94 nm, before the heat treatment.

The thermal stability may be attributable to a Zener pinning effect derived from the presence of dispersed nanoparticles. A maximum mean grain size can be theoretically estimated by

$$D_{max} = \frac{4r}{3f_v}$$

where r is the nanoparticle radius and f_v is the volume fraction of the nanoparticles. The D_{max} for Cu-34%WC is estimated to be 392 nm,

which is comparable with our experimental data. When compared with other precipitate particles from alloy systems, the ex situ WC nanoparticles will not dissolve in the Cu matrix at high temperatures, offering a superior thermal stability than conventional alloys.

Mechanical properties

The presence of fine, well-dispersed nanoparticles in a metal matrix is anticipated to significantly enhance mechanical responses (36–38). To gain fundamental insights into the property enhancement induced by the refined grains and nanoparticles, we conducted micropillar compression tests as shown in fig. S7. The typical micropillar of the Cu-WC sample with a diameter of 4 μm and a length of 9 μm is shown in fig. S7A, demonstrating that dense nanoparticles are dispersed in the micropillar. The polycrystalline nature of the micropillar is shown in fig. S7B. The typical results from the micropillar compression studies are shown in fig. S7C. The yield point increased from 180 ± 8 to 827 ± 74 MPa for pure Cu and as-solidified Cu-34vol%WC, respectively. Moreover, micropillars from Cu-34vol%WC sustained a gradually increasing load up to 1490 MPa and strain over 25% without catastrophic failure. In comparison, the pure Cu sample experienced extensive slip as the strain increases discontinuously. Furthermore, it is observed that the mechanical properties did not change much (yield point drops from 827 ± 74 to 780 ± 9) after a thermal exposure at 750°C for 2.0 hours, which further confirms that the Cu samples with WC nanoparticles exhibit excellent thermal stability. The detailed strengthening mechanisms are analyzed in the "Strengthening mechanisms" section of the Supplementary Materials. The Young's modulus of pure Cu, Cu-19vol%WC, and Cu-34vol%WC are measured by the nanoindentation method with a Berkovich tip. The Young's modulus of pure Cu, Cu-19vol%WC, and Cu-34vol%WC are 139 ± 8, 192 ± 13, and
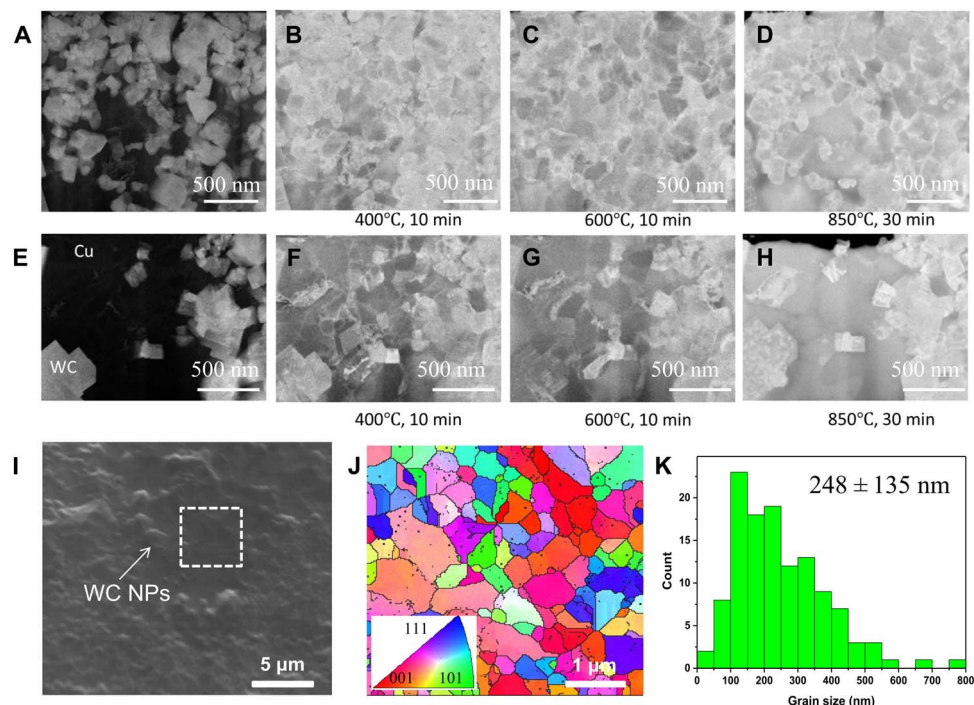

Fig. 4. Thermal stability of ultrafine/nanocrystalline Cu-containing WC nanoparticles. (**A** to **D**) STEM images of an area with a high percentage of WC nanoparticles at room temperature, 400°C, 600°C, and 850°C, respectively. (**E** to **H**) STEM image of an area with a relatively low percentage of WC nanoparticles at room temperature, 400°C, 600°C, and 850°C, respectively. (**I**) SEM image of Cu-34vol%WC after heat treatment (750°C for 2 hours). (**J**) EBSD image corresponds to the marked white rectangle in (I). (**K**) Cu grain size distribution of the heat-treated Cu-34vol%WC sample.

223 ± 16 GPa, respectively. We hypothesize that the enhancement of Young's modulus is due to the high Young's modulus of WC (~530 to 700 GPa) and the effective load transfer by the nanoparticles.

In summary, a revolutionary approach to effectively control nucleation and grain growth down to ultrafine/nanoscale during slow solidification was discovered using dispersed nanoparticles in molten metals. The nanoparticle-enabled new grain refinement mechanisms, which combine continuous nucleation and grain growth control, break the fundamental limit of conventional grain refinement methods. This new discovery enables a pathway to directly cast bulk UFG/nanocrystalline metals under slow cooling rates (e.g., less than 100 K/s) for large-scale production. An unprecedented thermal stability up to 1023 K, 0.75 T_m of Cu, for the as-cast bulk UFG/nanocrystalline Cu is demonstrated. As-cast bulk UFG/nanocrystalline metals with nanoparticles also show exceptional strengths and Young's modulus enhancement. Furthermore, this general approach is valid for different materials systems such as Al-TiB$_2$ and Zn-WC. This approach will have a profound impact not only on the solidification processes for metals but also on numerous applications such as biomedical, chemical, and atmospheric sciences.

MATERIALS AND METHODS
Materials fabrication
Salt-assisted incorporation method
WC nanoparticles were mixed with Borax (Na$_2$B$_4$O$_7$)–5wt%CaF$_2$ salt powders with a mechanical shaker (SK-O330-Pro) for 1 hour. The volume fraction of nanoparticles in the salt mixture was designed as 10%. As shown in fig. S1A, pure oxygen-free Cu (99.99%; RotoMetals Inc.) ingots were melted at 1250°C in a graphite crucible with an induction heater. Inert Ar gas was purged on the molten Cu to avoid severe oxidation. The mixed Na$_2$B$_4$O$_7$-5wt%CaF$_2$-WC nanoparticles were manually loaded on the surface of the molten Cu. A graphite propeller was located below the Cu-salt interface and stirred at a speed of 400 rpm for 20 min to incorporate WC nanoparticles into the Cu melt. Then, the melt was allowed to cool down to 900°C to allow Cu to solidify first, while salt mixture was still in the liquid state. Liquid salt was poured out from the crucible, and a Cu-WC ingot was left. The volume fraction of WC nanoparticles in Cu was designed to be 0, 5, 10, and 20 volume %.

Surface clean TiB$_2$ nanoparticles were synthesized by the magnesiothermic reduction of TiO$_2$ nanoparticles and B$_2$O$_3$ powders in molten salt (39). The synthesized TiB$_2$ nanoparticles and KAlF$_4$ flux were then mechanically mixed at the solid state for 3 hours. Mixed powders were dehydrated at 120°C for 1 hour in a vacuum oven. An electrical resistance furnace was used to melt the Al ingots at 820°C under argon (Ar) gas protection. Then, the mixed powders were added to the melt surface and melt was mechanically stirred at 200 rpm for 10 min with a titanium (Ti) mixing blade. The designed volume fraction of TiB$_2$ in Al is 10 volume %. The melt was taken out from the furnace and naturally cooled down to room temperature under Ar gas protection.
Powder melting method
Cu powders (<10 μm; Sigma-Aldrich) and Zn powders (150 μm; Alfa Aesar) were first mixed with a designed volume fraction of WC nanoparticles (150 to 200 nm; U.S. Research Nanomaterials) for 1 hour with a mechanical shaker (SK-O330-Pro). The mixed powders were then compressed into 2.0-cm-diameter discs under 250 MPa with a hydraulic machine. As shown in fig. S1B, Cu-WC cold compacted discs were compression-melted at 1250°C with an induction heater while un-

der a pressure of 7 to 10 MPa under a graphite disc and alumina piston. After solidification in air, Cu ingots with WC nanoparticles were obtained. Zn-WC cold compacted billets were then melted at 500°C and ultrasonically processed with a niobium (Nb) probe for 10 min to disperse WC nanoparticles in the Zn melt. Then, the melt was taken out from the furnace and cooled down under Ar gas protection.

Cooling rate measurement
To study the effects of the cooling rate, Cu-WC samples were melted again at 1250°C under argon gas protection and then cooled down in furnace, air, and water. The cooling rate was measured with a K-type thermocouple connected to an Arduino Uno board to record the cooling curve. The thermocouple was located at the center of the melt. The measured cooling rates of furnace cooling, air cooling, and water quenching are 2 to 4, 7 to 12, and 70 to 100 K/s, respectively. The typical cooling curves are shown in fig. S2, and the thermal arrest caused by the solidification of Cu is identified in the furnace and air cooling curve but is not obvious in the water quenching curve due to the rapid heat dissipation.

Structure characterization
The microstructure, distribution, and dispersion of nanoparticles in metals were studied by SEM, FIB imaging, EBSD, and TEM. To clean the surface and reveal the nanoparticles in the metal matrix, the mechanically grinded and polished as-cast samples were further polished by low-angle ion milling (model PIPS 691, Gatan). SEM images were acquired at 0° and 52° with Zeiss Supra 40VP and FEI Nova 600, respectively. The composition of the material was characterized by energy-dispersive x-ray spectroscopy. The volume fraction of nanoparticles was estimated on the basis of the atomic fraction of the major element in the base metal and nanoparticles. Taking advantage of the channeling contrast of different grains induced from the ion beam, FIB imaging was used to reveal the grain structure. Grain size and orientation were studied with EBSD (FEI Quanta 3D) at 30 kV with a current of 12 nA and FIB with a CDEM (channel detection electron multiplier) detector. The interfaces between the matrix and the nanoparticles were studied with an FEI Titan TEM at 300 kV. The thin-film TEM samples were machined with FIB.

Solidification behavior study
To study the solidification behaviors during cooling, Cu-WC and pure Cu samples with the same mass (50 mg) were analyzed using DSC (Q600, TA Instruments). Samples were heated up to 1250°C with a heating rate of 40°C/min and then cooled down with a cooling rate of 5°C/min.

High-temperature stability
To study the UFG/nanocrystalline structure stability at high temperatures, in situ heating STEM was conducted at 300 kV with a convergence angle of 4.3 mrad and geometric aberrations in the probe corrected to third order. The small convergence angle was chosen to enhance diffraction contrast for grain identification. An FIB-milled TEM sample was quickly heated to 200°, 400°, 600°, 700°, and 850°C with a Gatan in situ heating holder and held for 10 min at each step for imaging. The diffraction camera length was increased at higher temperatures to enhance diffraction contrast, emphasizing the difference between individual Cu grains for robust identification. The collection semiangle was 48 to 240 mrad at room temperature, 15 to 75 mrad at 400°C, and 12 to 60 mrad at 600°C and above. Moreover,

the bulk-solidified Cu-34vol%WC (air cooling, 7 K/s) samples were heated up to 750°C (1023 K, 0.75 of T_m) and stayed at that temperature for 2 hours under the protection of argon gas. The grain structure was then studied by FIB imaging and EBSD. Mechanical properties were studied by microcompression test.

Mechanical characterization and properties

A nanoindenter (MTS Systems Corporation) with a flat punch tip was used for microcompression tests at a strain rate of 5×10^{-2} s^{-1} under room temperature. Micropillars of approximately 4 µm in diameter and 9 µm in length were machined with FIB. To evaluate the elastic modulus, microindentation tests with an indent depth of 2 µm were performed by the same MTS nanoindenter with a Berkovich tip. For each sample, at least 10 points were measured. Accordingly, micropillars with a diameter of 4 µm and a length of 9 µm were machined with FIB from the as-solidified (air cooling, cooling rate of 7 K/s) and heat-treated samples (750°C for 2 hours).

SUPPLEMENTARY MATERIALS

Supplementary Text

Fig. S1. Fabrication of Cu-containing WC nanoparticles.

Fig. S2. Cooling curves for furnace cooling, air cooling, and water quenching of Cu-WC samples.

Fig. S3. Size distribution of WC nanoparticles in the as-solidified Cu-WC sample.

Fig. S4. Structure of bulk UFG/nanocrystalline Cu-containing WC nanoparticles.

Fig. S5. STEM image of the WC nanoparticle-rich area showing that the Cu grain size is correlated with WC interparticle spacing.

Fig. S6. Cooling curve during the DSC tests at a cooling rate of 5°C/min.

Fig. S7. Mechanical properties of UFG/nanocrystalline Cu-containing WC nanoparticles.

Fig. S8. Undercooling profile relative to solid fraction.

References (39–45)

REFERENCES AND NOTES

1. J. Kirkby, J. Curtius, J. Almeida, E. Dunne, J. Duplissy, S. Ehrhart, A. Franchin, S. Gagné, L. Ickes, A. Kürten, A. Kupc, A. Metzger, F. Riccobono, L. Rondo, S. Schobesberger, G. Tsagkogeorgas, D. Wimmer, A. Amorim, F. Bianchi, M. Breitenlechner, A. David, J. Dommen, A. Downard, M. Ehn, R. C. Flagan, S. Haider, A. Hansel, D. Hauser, W. Jud, H. Junninen, F. Kreissl, A. Kvashin, A. Laaksonen, K. Lehtipalo, J. Lima, E. R. Lovejoy, V. Makhmutov, S. Mathot, J. Mikkilä, P. Minginette, S. Mogo, T. Nieminen, A. Onnela, P. Pereira, T. Petäjä, R. Schnitzhofer, J. H. Seinfeld, M. Sipilä, Y. Stozhkov, F. Stratmann, A. Tomé, J. Vanhanen, Y. Viisanen, A. Vrtala, P. E. Wagner, H. Walther, E. Weingartner, H. Wex, P. M. Winkler, K. S. Carslaw, D. R. Worsnop, U. Baltensperger, M. Kulmala, Role of sulphuric acid, ammonia and galactic cosmic rays in atmospheric aerosol nucleation. Nature 476, 429–433 (2011).
2. A. Kiselev, F. Bachmann, P. Pedevilla, S. J. Cox, A. Michaelides, D. Gerthsen, T. Leisner, Active sites in heterogeneous ice nucleation—The example of K-rich feldspars. Science 355, 367–371 (2017).
3. M. L. Coombs, J. C. Eichelberger, M. J. Rutherford, Experimental and textural constraints on mafic enclave formation in volcanic rocks. J. Volcanol. Geotherm. Res. 119, 125–144 (2003).
4. M. H. Nielsen, S. Aloni, J. J. De Yoreo, In situ TEM imaging of CaCO3 nucleation reveals coexistence of direct and indirect pathways. Science 345, 1158–1162 (2014).
5. G. Frens, Controlled nucleation for the regulation of the particle size in monodisperse gold suspensions. Nature 241, 20–22 (1973).
6. R. Valiev, Nanostructuring of metals by severe plastic deformation for advanced properties. Nat. Mater. 3, 511–516 (2004).
7. Y.-H. Zhao, J. F. Bingert, X.-Z. Liao, B.-Z. Cui, K. Han, A. V. Sergueeva, A. K. Mukherjee, R. Z. Valiev, T. G. Langdon, Y. T. Zhu, Simultaneously increasing the ductility and strength of ultra-fine-grained pure copper. Adv. Mater. 18, 2949–2953 (2006).
8. L. Lu, Y. Shen, X. Chen, L. Qian, K. Lu, Ultrahigh strength and high electrical conductivity in copper. Science 304, 422–426 (2004).
9. A. L. Greer, Overview: Application of heterogeneous nucleation in grain-refining of metals. J. Chem. Phys. 145, 211704 (2016).
10. D. H. StJohn, M. Qian, M. Easton, P. Cao, Z. Hildebrand, Grain refinement of magnesium alloys. Metal. Mater. Trans. A 36, 1669–1679 (2005).
11. M. Easton, D. StJohn, An analysis of the relationship between grain size, solute content, and the potency and number density of nucleant particles. Metall. Mater. Trans. A 36, 1911–1920 (2005).
12. L.-Y. Chen, J.-Q. Xu, X.-C. Li, Controlling phase growth during solidification by nanoparticles. Mater. Res. Lett. 3, 43–49 (2015).
13. A. L. Greer, A. M. Bunn, A. Tronche, P. V. Evans, D. J. Bristow, Modelling of inoculation of metallic melts: Application to grain refinement of aluminium by Al–Ti–B. Acta Mater. 48, 2823–2835 (2000).
14. B. S. Murty, S. A. Kori, M. Chakraborty, Grain refinement of aluminium and its alloys by heterogeneous nucleation and alloying. Int. Mater. Rev. 47, 3–29 (2002).
15. Y. Birol, Grain refining efficiency of Al–Ti–C alloys. J. Alloys Compd. 422, 128–131 (2006).
16. D. H. StJohn, A. Prasad, M. A. Easton, M. Qian, The contribution of constitutional supercooling to nucleation and grain formation. Metal. Mater. Trans. A 46, 4868–4885 (2015).
17. S. Tamirisakandala, R. B. Bhat, J. S. Tiley, D. B. Miracle, Grain refinement of cast titanium alloys via trace boron addition. Scr. Mater. 53, 1421–1426 (2005).
18. C. Yu, T.-J. Zhu, K. Xiao, J.-J. Shen, S.-H. Yang, X.-B. Zhao, Reduced grain size and improved thermoelectric properties of melt spun (Hf, Zr) NiSn half-Heusler alloys. J. Electron. Mater. 39, 2008–2012 (2010).
19. Y. Wu, W. Han, S. X. Zhou, M. V. Lototsky, J. K. Solberg, V. A. Yartys, Microstructure and hydrogenation behavior of ball-milled and melt-spun Mg–10Ni–2Mm alloys. J. Alloys Compd. 466, 176–181 (2008).
20. C. Suryanarayana, Mechanical alloying and milling. Progr. Mater. Sci. 46, 1–184 (2001).
21. D. G. Morris, M. A. Morris, Microstructure and strength of nanocrystalline copper alloy prepared by mechanical alloying. Acta Metall. Mater. 39, 1763–1770 (1991).
22. R. Z. Valiev, Y. Estrin, Z. Horita, T. G. Langdon, M. J. Zechetbauer, Y. T. Zhu, Producing bulk ultrafine-grained materials by severe plastic deformation. JOM 58, 33–39 (2006).
23. D. S. Gianola, S. Van Petegem, M. Legros, S. Brandstetter, H. Van Swygenhoven, K. J. Hemker, Stress-assisted discontinuous grain growth and its effect on the deformation behavior of nanocrystalline aluminum thin films. Acta Mater. 54, 2253–2263 (2006).
24. G. Wu, K.-C. Chan, L. Zhu, L. Sun, J. Lu, Dual-phase nanostructuring as a route to high-strength magnesium alloys. Nature 545, 80–83 (2017).
25. L.-Y. Chen, J.-Q. Xu, H. Choi, H. Konishi, S. Jin, X.-C. Li, Rapid control of phase growth by nanoparticles. Nat. Commun. 5, 3879 (2014).
26. C. Cao, L. Chen, J. Xu, J. Zhao, M. Pozuelo, X. Li, Phase control in immiscible Zn-Bi alloy by tungsten nanoparticles. Mater. Lett. 174, 213–216 (2016).
27. C. Cao, W. Liu, Z. Liu, J. Xu, I. Hwang, I. De Rosa, X. Li, Scalable manufacturing of immiscible Al–Bi alloy by self-assembled nanoparticles. Mater. Des. 146, 163–171 (2018).
28. E. Guo, S. Shuai, D. Kazantsev, S. Karagadde, A. B. Phillion, T. Jing, W. Li, P. D. Lee, The influence of nanoparticles on dendritic grain growth in Mg alloys. Acta Mater. 152, 127–137 (2018).
29. N. Eustathopoulos, M. G. Nicholas, B. Drevet, Wettability at High Temperatures (Elsevier, 1999), vol. 3.
30. W. Liu, C. Cao, J. Xu, X. Wang, X. Li, Molten salt assisted solidification nanoprocessing of Al-TiC nanocomposites. Mater. Lett. 185, 392–395 (2016).
31. M. P. De Cicco, L.-S. Turng, X. Li, J. H. Perepezko, Nucleation catalysis in aluminum alloy A356 using nanoscale inoculants. Metall. Mater. Trans. A 42, 2323–2330 (2011).
32. M. A. Tschopp, H. A. Murdoch, L. J. Kecskes, K. A. Darling, "Bulk" nanocrystalline metals: Review of the current state of the art and future opportunities for copper and copper alloys. JOM 66, 1000–1019 (2014).
33. B. Wang, M. T. Alam, M. A. Haque, Grain growth in nanocrystalline nickel films at low temperature and stress. Scr. Mater. 71, 1–4 (2014).
34. K. A. Darling, M. Rajagopalan, M. Komarasamy, M. A. Bhatia, B. C. Hornbuckle, R. S. Mishra, K. N. Solanki, Extreme creep resistance in a microstructurally stable nanocrystalline alloy. Nature 537, 378–381 (2016).
35. T. Chookajorn, H. A. Murdoch, C. A. Schuh, Design of stable nanocrystalline alloys. Science 337, 951–954 (2012).
36. L.-Y. Chen, J.-Q. Xu, H. Choi, M. Pozuelo, X. Ma, S. Bhowmick, J.-M. Yang, S. Mathaudhu, X.-C. Li, Processing and properties of magnesium containing a dense uniform dispersion of nanoparticles. Nature 528, 539–543 (2015).
37. L.-Y. Chen, H. Konishi, A. Fehrenbacher, C. Ma, J.-Q. Xu, H. Choi, H.-F. Xu, F. E. Pfefferkorn, X.-C. Li, Novel nanoprocessing route for bulk graphene nanoplatelets reinforced metal matrix nanocomposites. Scr. Mater. 67, 29–32 (2012).
38. Y. Yang, J. Lan, X. Li, Study on bulk aluminum matrix nano-composite fabricated by ultrasonic dispersion of nano-sized SiC particles in molten aluminum alloy. Mater. Sci. Eng. A 380, 378–383 (2004).
39. A. Javadi, S. Pan, C. Cao, G. Yao, X. Li, Facile synthesis of 10 nm surface clean TiB2 nanoparticles. Mater. Lett. 229, 107–110 (2018).

40. B. J. Keene, Review of data for the surface tension of pure metals. *Int. Mater. Rev.* **38**, 157–192 (1993).

41. J. N. Israelachvili, *Intermolecular and Surface Forces* (Academic Press, 2011).

42. Z. Zhang, D. L. Chen, Consideration of Orowan strengthening effect in particulate-reinforced metal matrix nanocomposites: A model for predicting their yield strength. *Scr. Mater.* **54**, 1321–1326 (2006).

43. G. Liu, G. J. Zhang, F. Jiang, X. D. Ding, Y. J. Sun, J. Sun, E. Ma, Nanostructured high-strength molybdenum alloys with unprecedented tensile ductility. *Nat. Mater.* **12**, 344–350 (2013).

44. T. G. Nieh, J. Wadsworth, Hall-Petch relation in nanocrystalline solids. *Scr. Metall. Mater.* **25**, 955–958 (1991).

45. V. C. Nardone, K. M. Prewo, On the strength of discontinuous silicon carbide reinforced aluminum composites. *Scr. Metall.* **20**, 43–48 (1986).

Citation: C. Cao, G. Yao, L. Jiang, M. Sokoluk, X. Wang, J. Ciston, A. Javadi, Z. Guan, I. De Rosa, W. Xie, E. J. Lavernia, J. M. Schoenung, X. Li, Bulk ultrafine grained/nanocrystalline metals via slow cooling. *Sci. Adv.* **5**, eaaw2398 (2019).